



# Influence of Gd<sup>3+</sup>-substitution on structural, magnetic, dielectric and modulus spectroscopic characteristics of ZnFe<sub>2</sub>O<sub>4</sub> spinel ferrite nanoparticles

Raghvendra Singh Yadav<sup>1</sup> · Ivo Kuřitka<sup>1</sup> · Jarmila Vilcakova<sup>1</sup> · Jaromir Havlica<sup>2</sup> · Lukas Kalina<sup>2</sup> · Pavel Urbánek<sup>1</sup> · Michal Machovsky<sup>1</sup> · David Skoda<sup>1</sup> · Milan Masar<sup>1</sup>

Received: 24 April 2018 / Accepted: 13 July 2018 / Published online: 21 July 2018  
© Springer Science+Business Media, LLC, part of Springer Nature 2018

## Abstract

The gadolinium (Gd<sup>3+</sup>) substituted zinc ferrite nanoparticles (ZnFe<sub>2-x</sub>Gd<sub>x</sub>O<sub>4</sub>) for Gd<sup>3+</sup> (x = 0.00, 0.05, 0.10, 0.20) have been synthesized by honey mediated sol–gel auto-combustion method. The X-ray diffraction study revealed the formation of spinel ferrite crystal structure. The Raman spectroscopy and Fourier transform infrared spectroscopy study well support the XRD results analysis. The field emission scanning electron microscopy micrograph revealed spherical morphology and grain size around 10–30 nm for ZnFe<sub>2-x</sub>Gd<sub>x</sub>O<sub>4</sub> (x = 0.10) nanoparticles. The presence of Zn<sup>2+</sup> and Fe<sup>3+</sup> oxidation state in synthesized nanoparticles was confirmed by X-ray photoelectron spectroscopy. Magnetic properties of the Gd<sup>3+</sup> substituted zinc ferrite nanoparticles were investigated by vibrating sample magnetometer at room temperature. The conversion of magnetic hysteresis curves from ferromagnetic to a paramagnetic with the substitution of Gd<sup>3+</sup> in zinc ferrite nanoparticles was observed. Frequency dependent dielectric constant and ac conductivity measurements revealed that Gd<sup>3+</sup> substitution improved the value of dielectric constant and ac conductivity of the Gd<sup>3+</sup> substituted zinc ferrite nanoparticles. Further, the existence of two semicircles in Cole–Cole plot demonstrated the role of both grains and grain boundaries to conduction process in synthesized Gd<sup>3+</sup> ion substituted zinc ferrite nanoparticles. Furthermore, the grain relaxation time (τ<sub>g</sub>), grain boundary relaxation time (τ<sub>gb</sub>), grain resistance (R<sub>g</sub>), grain capacitance (C<sub>g</sub>), grain boundary resistance (R<sub>gb</sub>) and grain boundary capacitance (C<sub>gb</sub>) for synthesized ZnFe<sub>2-x</sub>Gd<sub>x</sub>O<sub>4</sub> (x = 0.00, 0.05, 0.10, 0.20) nanoparticles have been calculated using modulus spectroscopy analysis.

## 1 Introduction

Recently, spinel ferrite nanoparticles have attracted extensive attention due to their application, such as drug delivery, magnetic hyperthermia for cancer, magnetic resonance imaging, magnetic recording media, catalysis, sensor, microwave absorbers, telecommunications, electronics and electrical devices, etc. [1]. In general, spinel ferrite is represented by formula (M<sub>δ</sub>Fe<sub>1-δ</sub>)[M<sub>1-δ</sub>Fe<sub>1+δ</sub>]O<sub>4</sub>, where δ is known as cation distribution factor, and, the round and square brackets

represent the tetrahedral (A) and octahedral (B) sites [2]. Importantly, the physical characteristics such as magnetic, dielectric and electrical properties of spinel ferrite depend upon cation distribution factor. The cation distribution factor in spinel ferrite is dependent on preparation method, grain size, cation substitution, etc. [3]. Therefore, the physical properties of spinel ferrite can be regulated with substitution of rare-earth ions, i.e., the 4f element series, in partial replacement of Fe<sup>3+</sup> ions in spinel structure [4]. Recently, several researchers noticed change in physical characteristics of spinel ferrite nanoparticles with substitution of rare-earth ions [5–7]. However, few reports are available for Gd<sup>3+</sup> ion substitution in ZnFe<sub>2</sub>O<sub>4</sub> spinel ferrite nanoparticles and its physical characteristics [8, 9].

Recently, several synthesis techniques have been successfully adopted to synthesize rare-earth doped spinel ferrite nanoparticles, such as co-precipitation, microwave synthesis, sonochemical method, hydrothermal synthesis, solvothermal method, reverse micelles synthesis, sol–gel auto combustion

✉ Raghvendra Singh Yadav  
yadav@utb.cz; raghvendra.nac@gmail.com

<sup>1</sup> Centre of Polymer Systems, University Institute, Tomas Bata University in Zlín, Trida Tomase Bati 5678, 76001 Zlín, Czech Republic

<sup>2</sup> Materials Research Centre, Brno University of Technology, Purkyňova 464/118, 61200 Brno, Czech Republic

method, etc. [10–12]. Among these methods, sol–gel auto-combustion synthesis method has attracted great interest due to its capability to form highly crystalline, high purity, high homogeneity, and well controlled morphology of final product. To the best of our knowledge, there is no report available on  $Gd^{3+}$  substituted  $ZnFe_2O_4$  spinel ferrite nanoparticles prepared by green synthesis approach following the sol–gel auto-combustion synthesis technique. For industrial application, we need high quality spinel ferrite nanoparticles at mass scale level synthesized by green synthesis approach. In view of this, our research group adopted honey mediated sol–gel combustion method to synthesize gadolinium ( $Gd^{3+}$ ) doped zinc ferrite nanoparticles. The honey is used as a gelating and reducing agent in sol–gel auto-combustion method.

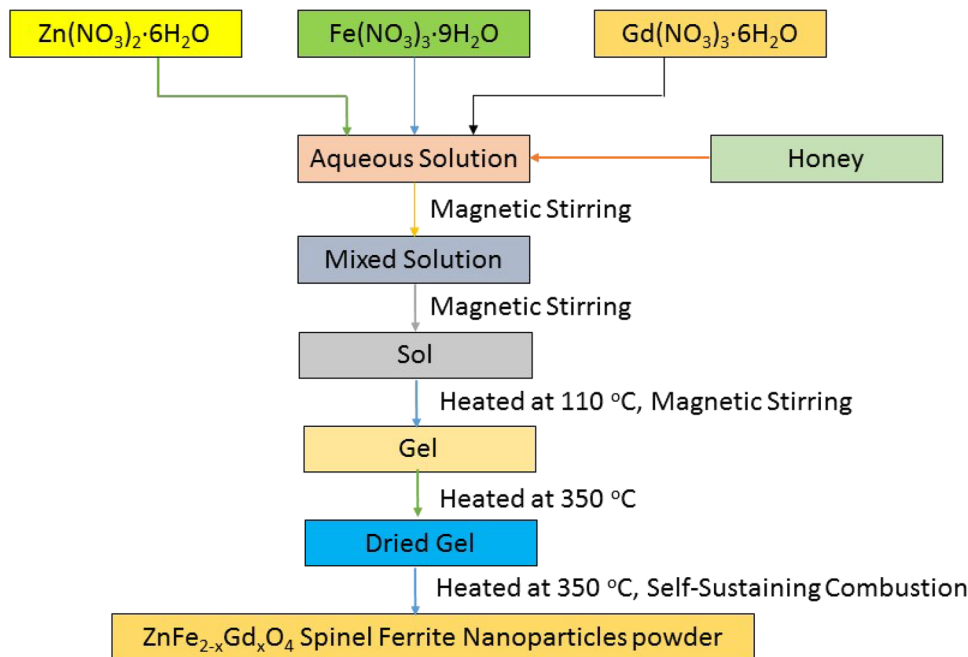
In the present work,  $ZnFe_{2-x}Gd_xO_4$  ( $x=0.00, 0.05, 0.10, 0.20$ ) spinel ferrite nanoparticles have been synthesized by honey mediated sol–gel auto-combustion method. Further, the influence of  $Gd^{3+}$  on structural, magnetic, dielectric, electrical and modulus spectroscopy characteristics have been studied in details. The  $Gd^{3+}$  substitution has significant influence on the grain growth, crystallite size, cation distribution and structural characteristics of synthesized spinel ferrite nanoparticles. The magnetic properties of synthesized spinel ferrite nanoparticles have been influenced by  $Gd^{3+}$  substitution. The frequency dependence dielectric constant and ac conductivity have been enhanced with the increase of  $Gd^{3+}$  concentration in zinc ferrite nanoparticles and it is maximum at  $x=0.10$ .

## 2 Experimental section

The gadolinium ( $Gd^{3+}$ ) substituted zinc ferrite nanoparticles were prepared *via* honey mediated sol–gel combustion method. For synthesis, analytical grade zinc nitrate [ $Zn(NO_3)_2 \cdot 6H_2O$ ], iron nitrate [ $Fe(NO_3)_3 \cdot 9H_2O$ ], and gadolinium nitrate [ $Gd(NO_3)_3 \cdot 6H_2O$ ] were procured from Alfa Aesar GmbH & Co KG, Germany. Honey was acquired from Tesco Stores Ltd. Cheshunt, EN8 9SL, U.K. The stoichiometric ratio of starting precursors (zinc nitrate, iron nitrate, and gadolinium nitrate) were dissolved in deionized water. The molar ratio of zinc nitrate to iron nitrate and gadolinium nitrate was 1:2. Thereafter, an aqueous solution of honey was added in above starting precursors solution. This prepared solution was kept on a hot plate with continuous stirring at 110 °C. After few minutes with evaporation of water, the mixed solution started to form a very viscous gel. Furthermore, this formed gel was heated to 350 °C to initiate a self-sustaining combustion reaction and produce final spinel ferrite nanoparticles powder. A series of  $ZnFe_{2-x}Gd_xO_4$  ( $x=0.00, 0.05, 0.10, 0.20$ ) nanoparticles were prepared by following above synthesis protocol (Fig. 1). The prepared powders were thoroughly ground in a mortar and then utilized for further characterizations and physical property measurements.

The grain, morphology, and elemental analysis of the  $Gd^{3+}$  doped zinc ferrite nanoparticles were analysed using scanning electron microscope Nova NanoSEM450 (FEI company) equipped with energy dispersive X-ray spectroscopy (EDX). An X-ray diffraction instrument Rigaku

**Fig. 1** Schematic representation of synthesis procedure for  $ZnFe_{2-x}Gd_xO_4$  nanoparticles synthesized by sol–gel combustion method



MiniFlex 600 X-ray Spectrometer (with a filtered cobalt source) was used to characterize crystal structure property of synthesized  $\text{Gd}^{3+}$  doped zinc ferrite nanoparticles. The magnetic characteristics of  $\text{Gd}^{3+}$  substituted zinc ferrite nanoparticles were studied by vibrating sample magnetometer (VSM 7407) at room temperature. The Infrared (IR) spectra of all prepared spinel ferrite samples were investigated by FTIR spectrometer Nicolet 6700 from Thermo Scientific. Raman spectroscopy characteristics of nanoparticles were characterized by dispersive Raman microscope Nicolet DXR. The presence of  $\text{Zn}^{2+}$  and  $\text{Fe}^{3+}$  ions in synthesized spinel ferrite nanoparticles were investigated by X-ray photoelectron spectroscopy (XPS) from Kratos Axis Ultra DLD. The dielectric and electrical characteristics of synthesized nanoparticles were investigated by a Broadband Dielectric Impedance Analyzer Concept 40.

### 3 Result and discussion

#### 3.1 Structural study

X-ray diffraction (XRD) pattern of synthesized  $\text{Gd}^{3+}$  substituted zinc ferrite nanoparticles are depicted in Fig. 2. The XRD pattern of  $\text{ZnFe}_{2-x}\text{Gd}_x\text{O}_4$  ( $x = 0.00, 0.05, 0.10, 0.20$ ) nanoparticles exhibit cubic spinel ferrite crystal structure. The observed XRD patterns are indexed as (220), (311), (222), (400), (422), (511) and (440), which confirm formation of cubic spinel ferrite structure [13]. The presence of iron oxide  $\text{Fe}_2\text{O}_3$  crystal phase can also be remarked from Fig. 2, which is represented as additional unindexed diffraction peaks [14]. We can also perceive from Fig. 2 that, with an increase of  $\text{Gd}^{3+}$  content 'x' the diffraction peak intensities were lessened and the full width at half maximum (FWHM) broadened, which signpost a decrease of crystallite size. The average crystallite size was deliberated from the

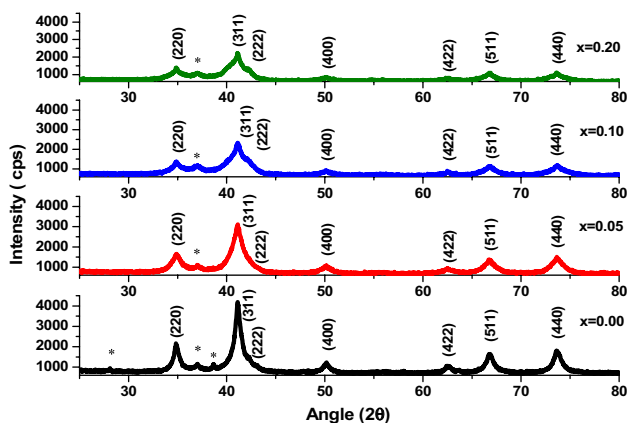


**Fig. 2** X-ray diffraction pattern of  $\text{ZnFe}_{2-x}\text{Gd}_x\text{O}_4$  ( $x = 0.00, 0.05, 0.10, 0.20$ ) spinel ferrite nanoparticles

line width of the (311) diffraction peak by using Scherrer's equation [15]:

$$D = \frac{0.94\lambda}{\beta \cos \theta}$$

where  $D$  is crystallite size,  $\lambda$  is the wavelength of Co  $K\alpha$  radiation ( $1.78897 \text{ \AA}$ ),  $\beta$  is the full width at half maximum (FWHM), and  $\theta$  is the diffraction angle. The calculated crystallite size for  $\text{ZnFe}_{2-x}\text{Gd}_x\text{O}_4$  ( $x = 0.00, 0.05, 0.10, 0.20$ ) nanoparticles are presented in Table 1. It can be remarked that the crystallite size decreases from 9.2 to 3.6 nm with an increase of  $\text{Gd}^{3+}$  content 'x' from 0.00 to 0.20, which signposts that the substitution of  $\text{Gd}^{3+}$  ions into  $\text{ZnFe}_2\text{O}_4$  spinel ferrite nanoparticles restrained the lattice growth of nanocrystalline particles [16]. Since the bond energy of  $\text{Gd-O}$  ( $719 \text{ kJ mol}^{-1}$ ) is higher as compared to bond energy  $\text{Fe-O}$  ( $390.4 \text{ kJ mol}^{-1}$ ) [17], as a result, more energy is desired for substitution of  $\text{Gd}^{3+}$  at the octahedral site in zinc ferrite. During synthesis, this additional needed energy is received at the expense of crystallization and thereby restriction in the growth of crystallite of zinc ferrite. Due to this, there is formation of smaller crystallite size of ferrite nanoparticle with an increase of  $\text{Gd}^{3+}$  content. The lattice constant 'a' of a cubic spinel structure was deliberated by following equation:

$$a = d\sqrt{h^2 + k^2 + l^2}$$

where (h k l) are the Miller indices and 'd' is inter-planar spacing. The assessed lattice constant for  $\text{ZnFe}_{2-x}\text{Gd}_x\text{O}_4$  ( $x = 0.00, 0.05, 0.10, 0.20$ ) nanoparticles are tabularised in Table 1, and it can be remarked that the lattice parameter decreases from 8.474 to 8.446  $\text{\AA}$ , almost linearly with the increase of  $\text{Gd}^{3+}$  content, which approves with Vegard's law. The ionic radii of  $\text{Gd}^{3+}$  (0.94  $\text{\AA}$ ) is larger than ionic radii of  $\text{Fe}^{3+}$  (0.64  $\text{\AA}$ ) and  $\text{Gd}^{3+}$  ions replaced  $\text{Fe}^{3+}$  ions at octahedral site in zinc ferrite nanoparticles. The larger ionic radii lead to the lattice strain and disorder lattice structure and consequently change in lattice parameter can be noticed [10, 18]. Since the doping of  $\text{Gd}^{3+}$  induces structural distortion, therefore, Williamson–Hall equation is utilized to evaluate strain and crystallite size [19]. Consider the size and strain

**Table 1** Crystallite size by Debye–Scherrer method and Williamson–Hall method (D), strain ( $\epsilon$ ), lattice parameter (a), X-ray density ( $d_x$ ) for  $\text{ZnFe}_{2-x}\text{Gd}_x\text{O}_4$  ( $x = 0.00, 0.05, 0.10, 0.20$ ) spinel ferrite nanoparticles

| x    | D (nm)<br>Scherrer<br>method | D (nm)<br>W–H<br>method | Strain (W–H<br>method)<br>$\times 10^{-3}$ | a ( $\text{\AA}$ ) | $d_x$ ( $\text{g cm}^{-3}$ ) |
|------|------------------------------|-------------------------|--|--------------------|------------------------------|
| 0.00 | 9.2                          | 18.3                    | 1.57                                       | 8.474              | 5.26                         |
| 0.05 | 5.6                          | 8.2                     | –1.1                                       | 8.466              | 5.38                         |
| 0.10 | 4.2                          | 8.1                     | –2.78                                      | 8.458              | 5.51                         |
| 0.20 | 3.6                          | 4.4                     | –8.35                                      | 8.446              | 5.76                         |

effect, the Williamson–Hall equation for the actual broadening ( $\beta$ ) can be written as:

$$\beta = \beta_{\text{size}} + \beta_{\text{strain}} = (K\lambda/D \cos \theta) + 4\epsilon \tan \theta$$

where  $\beta$ ,  $\theta$ ,  $K$ ,  $\lambda$ ,  $D$  and  $\epsilon$  is the full width at half maximum, (fwhm), the diffraction angle, the Debye–Scherrer constant, the X-ray wavelength, the crystallite size and the micro-strain, respectively. Further, above equation can be written as:

$$\beta \cos \theta = K\lambda/D + 4\epsilon \sin \theta$$

A linear plot of  $\beta \cos \theta$  versus  $4 \sin \theta$  is used to evaluate the crystallite size through the intercept and the strain by its slope. The Williamson–Hall plots for  $\text{ZnFe}_{2-x}\text{Gd}_x\text{O}_4$  ( $x = 0.00, 0.05, 0.10, 0.20$ ) nanoparticles are shown in Fig. 3 and the evaluated value of crystallite size and micro-strain from the Williamson–Hall plots is presented in Table 1. The crystallite size of pure zinc ferrite was 18.3 nm and it was decreased with the addition of  $\text{Gd}^{3+}$  in spinel ferrite from 18.3 to 4.4 nm. It can be perceived that the slope for pure  $\text{ZnFe}_2\text{O}_4$  nanoparticles is positive, which remarks the existence of a small micro-strain in the lattice of the spinel structure. In addition, the slope of the plots changes from positive to negative and intercept values gradually decreases with increasing  $\text{Gd}^{3+}$  content in zinc ferrite nanoparticles. Further, the X-ray density was also evaluated for synthesized spinel ferrite nanoparticles according to the relation [20]:

$$d_x = 8M/\text{Na}^3$$

where  $M$ ,  $N$  and ‘ $a^3$ ’ is the molecular mass, Avogadro’s number and the volume of the cubic unit cell. The value of X-ray densities with an increase of  $\text{Gd}^{3+}$  content in zinc ferrite, is presented in Table 1 and it can be notice that the value of X-ray density increases with the  $\text{Gd}^{3+}$  ions substitution in the synthesized zinc ferrite nanoparticles. The higher

value of X-ray density is recognised to upgraded molecular weight of the spinel ferrite samples with gadolinium ions. The increased density represents that the particles have a tendency to acquire nano size and more tightly packed. Furthermore, the hopping length for tetrahedral site ( $d_A$ ), hoping length for octahedral site ( $d_B$ ), tetrahedral bond length ( $d_{Ax}$ ), octahedral bond length ( $d_{Bx}$ ), tetrahedral edge ( $d_{AxE}$ ), shared octahedral edge ( $d_{BxE}$ ) and unshared octahedral edge ( $d_{BxEU}$ ) for  $\text{ZnFe}_{2-x}\text{Gd}_x\text{O}_4$  ( $x = 0.00, 0.05, 0.10, 0.20$ ) nanoparticles were evaluated using values of lattice parameters ‘ $a$ ’, ‘ $u$ ’ the oxygen positional parameter, and substituting it into the following relations [21]:

$$d_A = 0.25a\sqrt{3}$$

$$d_B = 0.25a\sqrt{2}$$

$$d_{Ax} = a\sqrt{3}(u - 1/4)$$

$$d_{Bx} = a[3u^2 - (11/4)u + (43/64)]^{1/2}$$

$$d_{AxE} = a\sqrt{2}(2u - 1/2)$$

$$d_{BxE} = a\sqrt{2}(1 - 2u)$$

$$d_{BxEU} = a[4u^2 - 3u + (11/16)]^{1/2}$$

The calculated value of X-ray parameters for  $\text{ZnFe}_{2-x}\text{Gd}_x\text{O}_4$  ( $x = 0.00, 0.05, 0.10, 0.20$ ) nanoparticles are presented in Table 2 and it can be perceived that tetrahedral bond length, octahedral bond length, tetrahedral edge, shared and unshared octahedral edges decreased with the increase of  $\text{Gd}^{3+}$  content in zinc ferrite nanoparticles. It can be also remarked that the hopping length  $d_A$  and  $d_B$  decreases with  $\text{Gd}^{3+}$  content increases in spinel ferrite nanoparticles. It has signposted that the distance between magnetic ions decreases as  $\text{Gd}^{3+}$  content increases. This could be related to the larger ionic radius of  $\text{Gd}^{3+}$  ion as compared with  $\text{Fe}^{3+}$  ion and cation redistribution among tetrahedral and octahedral site [21].

The cation distributions among the tetrahedral and octahedral sites in synthesized spinel ferrite nanoparticles were evaluated qualitatively by the Rietveld refinement of the occupancy values by using Fullprof Suite [22, 23]. Figure 4 indicate typical XRD pattern along with the Rietveld refinements for  $\text{ZnFe}_{2-x}\text{Gd}_x\text{O}_4$  ( $x = 0.10$ ) spinel ferrite nanoparticles. The fractional atomic coordinates of the atoms used in the refinement for  $\text{ZnFe}_{2-x}\text{Gd}_x\text{O}_4$  ( $x = 0.00, 0.05, 0.10, 0.20$ ) nanoparticles are tabulated in Table 3 along with the occupancy. In the refinement, the oxygen positions ( $X = Y = Z$ ) were taken as

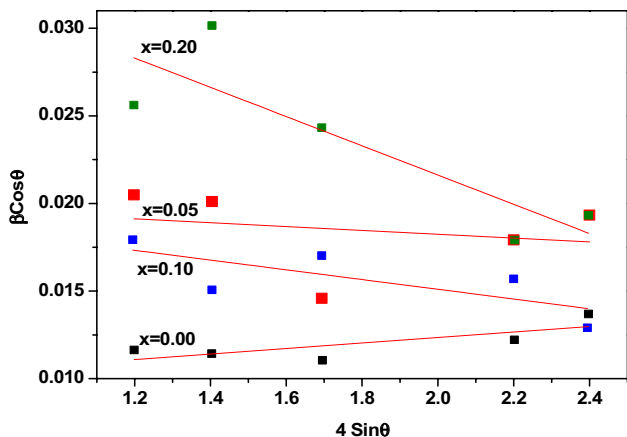
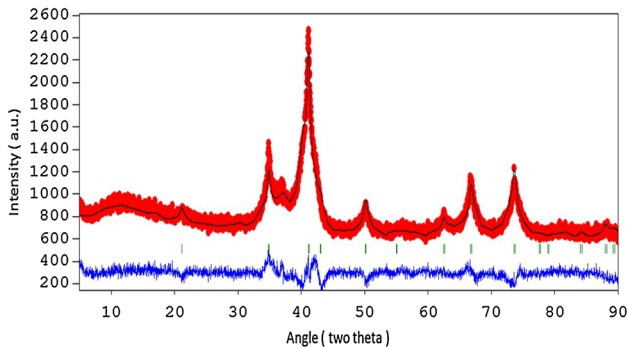


Fig. 3 Williamson–Hall plots for  $\text{ZnFe}_{2-x}\text{Gd}_x\text{O}_4$  ( $x = 0.00, 0.05, 0.10, 0.20$ ) spinel ferrite nanoparticles

**Table 2** The hopping length for tetrahedral site ( $d_A$ ), hoping length for octahedral site ( $d_B$ ), tetrahedral bond length ( $d_{Ax}$ ), octahedral bond length ( $d_{Bx}$ ), tetrahedral edge ( $d_{AxE}$ ), shared octahedral edge ( $d_{BxE}$ ) and unshared octahedral edge ( $d_{BxEU}$ ) for  $ZnFe_{2-x}Gd_xO_4$  ( $x = 0.00, 0.05, 0.10, 0.20$ ) spinel ferrite nanoparticles

| x    | $d_A$ (Å) | $d_B$ (Å) | $d_{Ax}$ (Å) | $d_{Bx}$ (Å) | $d_{AxE}$ (Å) | $d_{BxE}$ (Å) | $d_{BxEU}$ (Å) |
|------|-----------|-----------|--------------|--------------|---------------|---------------|----------------|
| 0.00 | 3.6692    | 2.9956    | 1.9226       | 2.0688       | 3.1393        | 2.8517        | 2.9976         |
| 0.05 | 3.6657    | 2.9927    | 1.9208       | 2.0668       | 3.1363        | 2.8490        | 2.9948         |
| 0.10 | 3.6623    | 2.9899    | 1.9190       | 2.0649       | 3.1334        | 2.8463        | 2.9920         |
| 0.20 | 3.6571    | 2.9856    | 1.9163       | 2.0619       | 3.1289        | 2.8423        | 2.9877         |



**Fig. 4** Rietveld refined XRD pattern for  $ZnFe_{2-x}Gd_xO_4$  ( $x = 0.10$ ) spinel ferrite nanoparticles

free parameters, however, all other atomic fractional positions were taken as fixed. Moreover, other parameters such as lattice constants, occupancies, scale factors, and shape parameters were taken as free parameters. The background was corrected by pseudo-voigt function. The evaluated cation distribution, lattice constant ( $a$ ), unit cell volume ( $V$ ), and density ( $d$ ) from Rietveld analysis for synthesized spinel ferrite nanoparticles

is tabulated in Table 4. The cation distribution evaluated from Rietveld analysis indicates that  $Gd^{3+}$  ions occupy octahedral sites. Further, the cation distribution evaluated from Rietveld analysis indicates that Zn and Fe ions occupy both tetrahedral and octahedral sites, therefore, the synthesized nanoparticles are in mixed spinel structure. Furthermore, with the substitution  $Gd^{3+}$  in zinc ferrite nanoparticles, there is redistribution of cations at octahedral and tetrahedral sites. The cation redistribution is associated with variation in lattice constant.

The bond length between cations–cations ( $M_e-M_e$ ) and cations–anions ( $Me-O$ ) (Fig. 5) can be evaluated using the following relations [24]:

$$b = \sqrt{2} (a/4)$$

$$c = \sqrt{11} (a/8)$$

$$d = \sqrt{3} (a/4)$$

$$e = \sqrt{3} (3a/8)$$

**Table 3** Typical atomic coordinates ( $X, Y, Z$ ) and occupancy of different atoms for  $ZnFe_{2-x}Gd_xO_4$  ( $x = 0.00, 0.05, 0.10, 0.20$ ) nanoparticles

| Atoms    | Coordinate |        |        | Occupancy |       |       |       |
|----------|------------|--------|--------|-----------|-------|-------|-------|
|          | X          | Y      | Z      | 0.00      | 0.05  | 0.10  | 0.20  |
| Fe (8a)  | 0.1250     | 0.1250 | 0.1250 | 0.385     | 0.395 | 0.404 | 0.631 |
| Zn (8a)  | 0.1250     | 0.1250 | 0.1250 | 0.499     | 0.596 | 0.496 | 0.477 |
| Fe (16d) | 0.5000     | 0.5000 | 0.5000 | 1.615     | 1.559 | 1.502 | 1.172 |
| Zn (16d) | 0.5000     | 0.5000 | 0.5000 | 0.501     | 0.404 | 0.504 | 0.523 |
| Gd (16d) | 0.5000     | 0.5000 | 0.5000 | 0.000     | 0.046 | 0.094 | 0.197 |
| O (32e)  | –          | –      | –      | 4.000     | 4.000 | 4.000 | 4.000 |

**Table 4** Results obtained from Rietveld analysis: site occupancies of cations, lattice constant  $a$ , unit cell volume  $V$ , and density  $d$  for  $ZnFe_{2-x}Gd_xO_4$  ( $x = 0.00, 0.05, 0.10, 0.20$ ) nanoparticles

| Composition, x | Cation distribution        |                                      | $a$ (Å) | $V$ (Å <sup>3</sup> ) | $d$ (g cm <sup>-3</sup> ) |
|----------------|----------------------------|--------------------------------------|---------|-----------------------|---------------------------|
|                | Tetrahedral (A) site       | Octahedral (B) site                  |         |                       |                           |
| 0.00           | ( $Zn_{0.499}Fe_{0.385}$ ) | [ $Zn_{0.501}Fe_{1.615}$ ]           | 8.485   | 610.88                | 5.24                      |
| 0.05           | ( $Zn_{0.596}Fe_{0.395}$ ) | [ $Zn_{0.404}Fe_{1.559}Gd_{0.046}$ ] | 8.478   | 609.37                | 5.37                      |
| 0.10           | ( $Zn_{0.496}Fe_{0.404}$ ) | [ $Zn_{0.504}Fe_{1.502}Gd_{0.094}$ ] | 8.452   | 603.78                | 5.53                      |
| 0.20           | ( $Zn_{0.477}Fe_{0.631}$ ) | [ $Zn_{0.523}Fe_{1.172}Gd_{0.197}$ ] | 8.442   | 601.64                | 5.77                      |

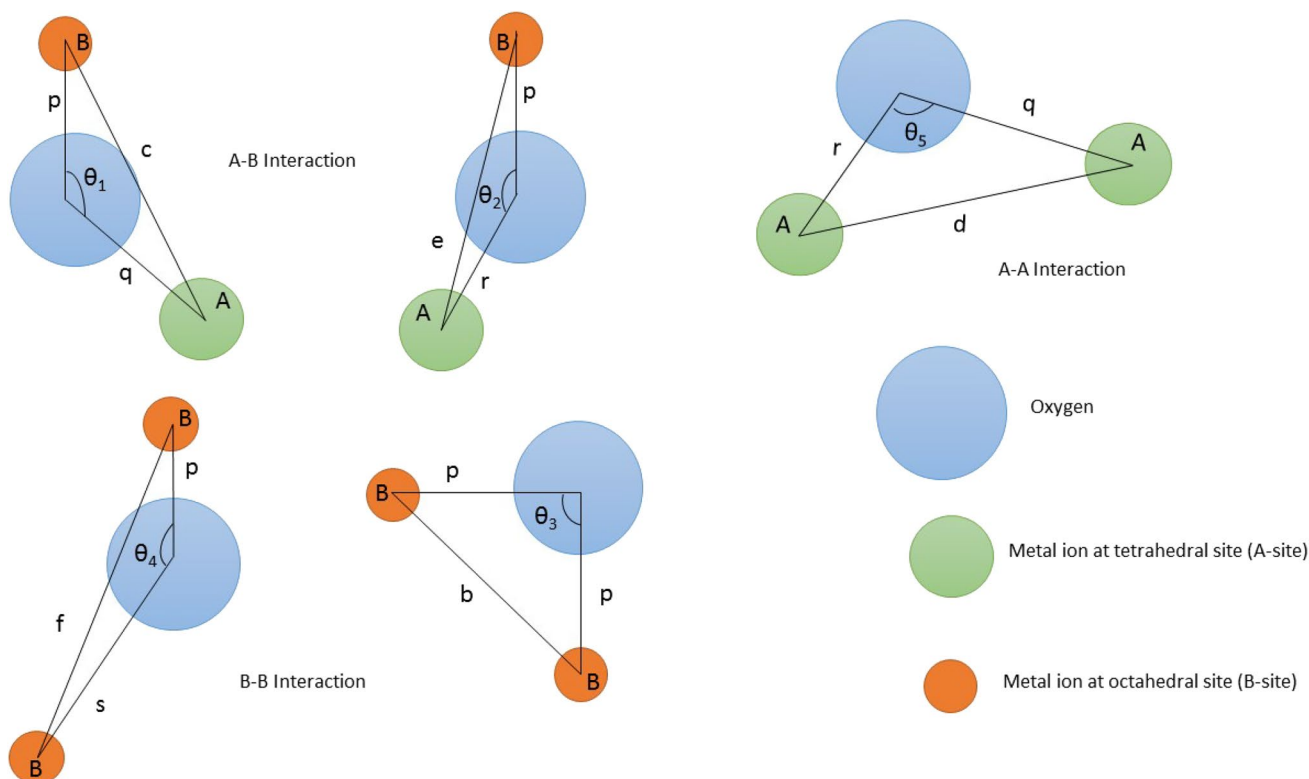


Fig. 5 Ion pair configuration in spinel ferrite with bond lengths and bond angles

$$f = \sqrt{6}(a/4)$$

$$p = a(5/8 - u)$$

$$q = a\sqrt{3}(u - 1/4)$$

$$r = a\sqrt{11}(u - 1/8)$$

$$s = a\sqrt{3}(u/3 + 1/8)$$

The evaluated value of bond length between cations–cations and cations–anions is tabulated in Table 5. Further, the bond angles between cations–cations and cations–anions (Fig. 5) can be evaluated by using following relations [25]:

$$\theta_1 = \cos^{-1}\left(\frac{p^2 + q^2 - c^2}{2pq}\right)$$

$$\theta_2 = \cos^{-1}\left(\frac{p^2 + r^2 - e^2}{2pr}\right)$$

Table 5 Bond lengths between cations–cations ( $M_c-M_c$ ), cations–anions ( $M_c-O$ ) and bond angles of  $ZnFe_{2-x}Gd_xO_4$  ( $x=0.00, 0.05, 0.10, 0.20$ ) nanoparticles

| Bond lengths and bond angles | x=0.00   | x=0.05   | x=0.10   | x=0.20   |
|------------------------------|----------|----------|----------|----------|
| $M_c-M_c$ (Å)                |          |          |          |          |
| b                            | 2.9994   | 2.9969   | 2.9877   | 2.9842   |
| c                            | 3.5176   | 3.5147   | 3.5039   | 3.4998   |
| d                            | 3.6740   | 3.6709   | 3.6597   | 3.6554   |
| e                            | 5.5110   | 5.5065   | 5.4896   | 5.4831   |
| f                            | 5.1960   | 5.1917   | 5.1758   | 5.1697   |
| $M_c-O$ (Å)                  |          |          |          |          |
| p                            | 2.0703   | 2.0686   | 2.0623   | 2.0598   |
| q                            | 1.9252   | 1.9236   | 1.9177   | 1.9154   |
| r                            | 3.6865   | 3.6834   | 3.6722   | 3.6678   |
| s                            | 3.7034   | 3.7003   | 3.6889   | 3.6846   |
| Angles (degree)              |          |          |          |          |
| $\theta_1$                   | 123.3413 | 123.3410 | 123.3414 | 123.3412 |
| $\theta_2$                   | 144.9378 | 144.9376 | 144.9380 | 144.9367 |
| $\theta_3$                   | 92.8355  | 92.8354  | 92.8358  | 92.8354  |
| $\theta_4$                   | 125.9242 | 125.9243 | 125.9243 | 125.9239 |
| $\theta_5$                   | 74.4789  | 74.4785  | 74.4789  | 74.4785  |

$$\theta_3 = \cos^{-1} \left( \frac{2p^2 - b^2}{2p^2} \right)$$

$$\theta_4 = \cos^{-1} \left( \frac{p^2 + s^2 - f^2}{2ps} \right)$$

$$\theta_5 = \cos^{-1} \left( \frac{r^2 + q^2 - d^2}{2rq} \right)$$

The calculated value of bond angles between cations–cations and cations–anions is mentioned in Table 5. The variation in bond length and bond angles was associated with substitution of  $Gd^{3+}$  in zinc ferrite nanoparticles.

### 3.2 FTIR spectroscopy

Fourier transform infrared spectroscopy is an important structural characterization tool to investigate the position of ions involved in the crystal lattice based on their vibrational modes [26]. Figure 6 represents the Fourier transform infrared spectra of spinel ferrite  $ZnFe_{2-x}Gd_xO_4$  ( $x = 0.00, 0.05, 0.10, 0.20$ ) nanoparticles. In spinel ferrite, the metal ion occupies two different sub-lattices named as tetrahedral (A-site) and octahedral (B-site) positions with respect to the geometrical configuration of the oxygen nearest neighbours [27]. It can be noticed from Fig. 6 that there are two main characteristic absorption bands of spinel structure [28]. The highest absorption band around  $525\text{--}535\text{ cm}^{-1}$  is associated with stretching vibration of metal at the tetrahedral site, whereas the lowest band around  $350\text{--}360\text{ cm}^{-1}$  is related to stretching vibration of the octahedral site [29]. The presence of  $\nu_1$  and  $\nu_2$  absorption bands approve the formation of the spinel ferrite crystal structure of  $Gd^{3+}$  substituted  $ZnFe_2O_4$

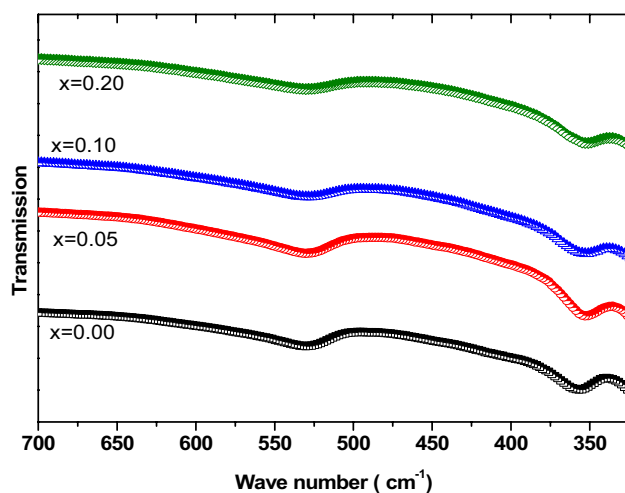


**Fig. 6** FTIR spectra of  $ZnFe_{2-x}Gd_xO_4$  ( $x = 0.00, 0.05, 0.10, 0.20$ ) nanoparticles

nanoparticles. It can be noted that the difference in absorption bands  $\nu_1$  and  $\nu_2$  is related to change of bond length (Fe–O) at the octahedral and tetrahedral site [30]. It can be also observed from Fig. 6 and Table 6 that the tetrahedral and octahedral characteristic absorption band shifted to lower wavenumber with an increase of substitution of  $Gd^{3+}$  content in zinc ferrite nanoparticles. The substitution of higher ion  $Gd^{3+}$  in place of lighter ion  $Fe^{3+}$  resulted from the shift in characteristic absorption band to a lower wavenumber [31]. Further, the shift in absorption band position is also related to cation redistribution or migration among tetrahedral and octahedral sites in  $Gd^{3+}$  substituted  $ZnFe_2O_4$  nanoparticles [32]. The force constant ( $k$ ) has relation with the frequency of vibrational mode ( $\nu$ ), which can be express by the following relation [33]:

$$\nu = \frac{1}{2\pi c} \sqrt{\frac{k}{m}}$$

where  $c$ ,  $\nu$ ,  $m$  and  $k$  are the velocity of light, the frequency of vibrational mode, mass of the vibrating atoms and the force constant, respectively. The force constant for the tetrahedral site ( $k_T$ ) and octahedral site ( $k_O$ ) was evaluated using the frequency absorption band  $\nu_1$  and  $\nu_2$ . The evaluated values of force constant for  $ZnFe_{2-x}Gd_xO_4$  ( $x = 0.00, 0.05, 0.10, 0.20$ ) nanoparticles are tabulated in Table 6. The value of force constant decreases with the substitution of  $Gd^{3+}$  in zinc ferrite nanoparticles. The change in force constant is associated with the variation in bond length of cations and oxygen ion at the octahedral and tetrahedral site in synthesized  $Gd^{3+}$  substituted zinc ferrite nanoparticles [34].

### 3.3 Raman spectroscopy

Raman spectroscopy is utilized to reveal the information associated with crystal structural change due to  $Gd^{3+}$  substitution in zinc ferrite nanoparticles [35]. Figure 7 depicts the room temperature Raman spectra of  $ZnFe_{2-x}Gd_xO_4$  ( $x = 0.00, 0.05, 0.10, 0.20$ ) nanoparticles in the range of  $200\text{--}800\text{ cm}^{-1}$ . A theoretical study predicts the following optical modes for spinel ferrite system:

**Table 6** Vibrational bands ( $\nu_1$  and  $\nu_2$ ), force constant ( $k_T$  and  $k_O$ ) and band gap for spinel ferrite  $ZnFe_{2-x}Gd_xO_4$  ( $x = 0.00, 0.05, 0.10, 0.20$ ) nanoparticles

| x    | FTIR bands ( $\text{cm}^{-1}$ ) |         | Force constant ( $\times 10^2\text{ N/m}$ ) |       |
|------|---------------------------------|---------|---|-------|
|      | $\nu_1$                         | $\nu_2$ | $k_T$                                       | $k_O$ |
| 0.00 | 531                             | 356     | 2.07  | 0.93  |
| 0.05 | 530                             | 354     | 2.06  | 0.92  |
| 0.10 | 529                             | 353     | 2.05  | 0.91  |
| 0.20 | 527                             | 350     | 2.03  | 0.89  |

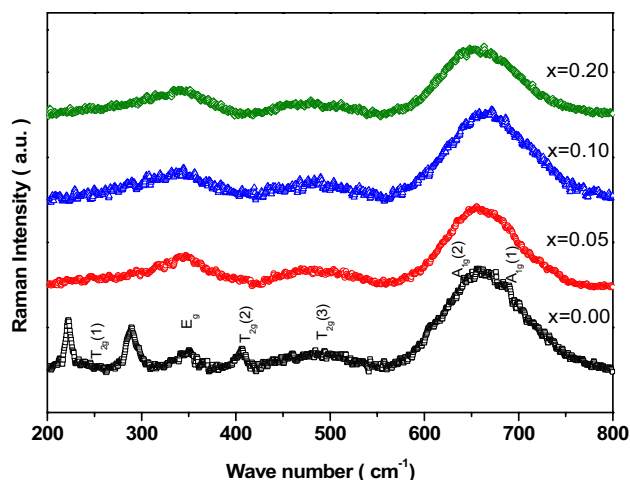


**Fig. 7** Raman spectra of spinel ferrite  $\text{ZnFe}_{2-x}\text{Gd}_x\text{O}_4$  ( $x=0.00, 0.05, 0.10, 0.20$ ) nanoparticles

$5T_{1u} + A_{1g} + E_g + 3T_{2g}$  [36]. In which  $5T_{1u}$  modes are IR active, whereas other five modes ( $A_{1g} + E_g + 3T_{2g}$ ) are Raman active modes consisted of motion of O ions and both the tetrahedral and octahedral site ions in the spinel ferrite crystal structure [37]. Here, the  $A_{1g}$  mode is due to the symmetric stretching of the oxygen anion, whereas the  $E_g$  mode is the result of symmetric bending of the oxygen anion, whereas, the  $T_{2g}$  mode is because of asymmetric stretching of the oxygen anion with respect to the tetrahedral and octahedral site cations [38]. For pure zinc ferrite nanoparticles, Raman spectra consist of Raman modes at 243, 349, 406, 499, 659, 686  $\text{cm}^{-1}$ , as presented in Table 7. It is also evident from Fig. 7 that the Raman mode around 686  $\text{cm}^{-1}$  shows a shoulder like a feature at the lower wavenumber side around 659  $\text{cm}^{-1}$  [39]. These Raman modes were represented to  $A_{1g}(1)$  and  $A_{1g}(2)$  modes, which are associated with the stretching vibration of iron–oxygen and metal–oxygen chemical bonds at tetrahedral sites. Furthermore, the other low-frequency modes (243, 349, 406, 499  $\text{cm}^{-1}$ ) were represented to the  $T_{2g}$  and  $E_g$  modes, which represent the vibration of the spinel structure. The presence of additional Raman bands at around 222 and 290  $\text{cm}^{-1}$  in pure zinc ferrite nanoparticles is associated with  $\alpha\text{-Fe}_2\text{O}_3$  phase [40]. These bands related to  $\alpha\text{-Fe}_2\text{O}_3$  phase were disappeared with

the substitution of  $\text{Gd}^{3+}$  in zinc ferrite nanoparticles. The change in the Raman bands with the substitution of  $\text{Gd}^{3+}$  content ‘ $x$ ’ in zinc ferrite nanoparticles is related to the larger ionic radius of  $\text{Gd}^{3+}$  ion as compared with  $\text{Fe}^{3+}$  ion and cation redistribution among tetrahedral and octahedral site [41].

### 3.4 FE-SEM and EDX study

Typical field emission scanning electron microscopy (FE-SEM) image and energy dispersive X-ray spectroscopy (EDX) spectrum of  $\text{ZnFe}_{2-x}\text{Gd}_x\text{O}_4$  ( $x=0.10$ ) nanoparticles are presented in Fig. 8. As shown in Fig. 8a,  $\text{ZnFe}_{2-x}\text{Gd}_x\text{O}_4$  ( $x=0.10$ ) nanoparticles have spherical morphology and grain size around 10–30 nm. By observation of EDX spectrum of these particles (Fig. 8b), only Zn, Fe, Gd, and O are detected, which further confirm the formation of  $\text{ZnFe}_{2-x}\text{Gd}_x\text{O}_4$  ( $x=0.10$ ) nanoparticles.

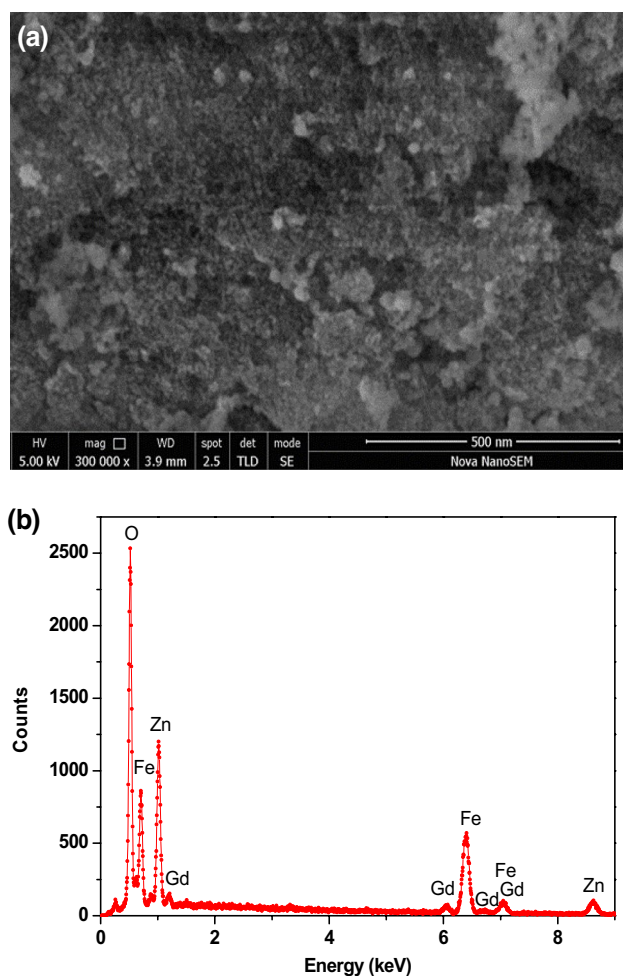
### 3.5 X-ray photoelectron spectroscopy

Figure 9 illustrates high resolution X-ray photoelectron spectroscopy (XPS) spectra of Zn and Fe for spinel ferrite  $\text{ZnFe}_{2-x}\text{Gd}_x\text{O}_4$  ( $x=0.00$  and 0.20) nanoparticles. Figure 9a depicts XPS spectra of Zn 2p for  $\text{ZnFe}_{2-x}\text{Gd}_x\text{O}_4$  ( $x=0.00$ ) nanoparticles, which consist of two peaks centered at 1043.3 and 1020.2 eV and it is associated with binding energy of Zn  $2p_{1/2}$  and Zn  $2p_{3/2}$ , respectively [42]. It indicates the oxidation state of  $\text{Zn}^{2+}$  in  $\text{ZnFe}_2\text{O}_4$  nanoparticles [43]. The peak Zn  $2p_{3/2}$  can be resolved into two peaks. These two peaks are due to two lattice sites for  $\text{Zn}^{2+}$  in spinel ferrite. The binding energy associated with  $\text{Zn}^{2+}$  ( $O_h$ ) and  $\text{Zn}^{2+}$  ( $T_h$ ) are 1020.2 and 1022.1 eV, respectively. Figure 9b depicts XPS spectra of Fe 2p for  $\text{ZnFe}_{2-x}\text{Gd}_x\text{O}_4$  ( $x=0.00$ ) nanoparticles, the main two peaks are noticed at 723.6 and 709.7 eV, which is related to the Fe  $2p_{1/2}$  and Fe  $2p_{3/2}$ , respectively [44]. The presence of satellite peaks at 718.6 and 732.0 eV can be also noticed from Fig. 9b, which is consistent with an oxidation state of  $\text{Fe}^{3+}$  in  $\text{ZnFe}_2\text{O}_4$  nanoparticles [45]. The peak Fe  $2p_{3/2}$  are resolved into two peaks, the binding energy associated with  $\text{Fe}^{3+}$  ( $O_h$ ) and  $\text{Fe}^{3+}$  ( $T_h$ ) are 709.4 and 711.5 eV. Similar results are also noticed for  $\text{ZnFe}_{2-x}\text{Gd}_x\text{O}_4$  ( $x=0.20$ ) nanoparticles (Fig. 9c, d), which confirm presence of  $\text{Zn}^{2+}$  and  $\text{Fe}^{3+}$  oxidation state.

**Table 7** Raman modes for spinel ferrite  $\text{ZnFe}_{2-x}\text{Gd}_x\text{O}_4$  ( $x=0.00, 0.05, 0.10, 0.20$ ) nanoparticles

| x    | Raman modes ( $\text{cm}^{-1}$ ) |             |             |             |       |             |
|------|----------------------------------|-------------|-------------|-------------|-------|-------------|
|      | $A_{1g}(1)$                      | $A_{1g}(2)$ | $T_{2g}(3)$ | $T_{2g}(2)$ | $E_g$ | $T_{2g}(1)$ |
| 0.00 | 686                              | 659         | 499         | 406         | 349   | 243         |
| 0.05 | 682                              | 655         | 486         | 408         | 345   | 244         |
| 0.10 | 680                              | 654         | 485         | 407         | 342   | 242         |
| 0.20 | 670                              | 647         | 477         | 411         | 337   | 240         |





**Fig. 8** **a** Scanning electron microscopy image and **b** EDS image of spinel ferrite ZnFe<sub>2-x</sub>Gd<sub>x</sub>O<sub>4</sub> (x = 0.10) nanoparticles

### 3.6 Magnetic property

Magnetic properties of synthesized Gd<sup>3+</sup> ion substituted zinc ferrite nanoparticles were investigated by Vibrating Sample Magnetometer (VSM) at room temperature. The magnetic characteristics of spinel ferrite materials depend on several factors, cation substitution, cation redistribution, grain size, synthesis method, etc. [46]. Figure 10 illustrates magnetic hysteresis curves for ZnFe<sub>2-x</sub>Gd<sub>x</sub>O<sub>4</sub> (x = 0.00, 0.05, 0.10, 0.20) nanoparticles. It can be noticed that zinc ferrite nanoparticles exhibit ferromagnetic to paramagnetic behavior with the increase of substitution of Gd<sup>3+</sup> content 'x'. Pure zinc ferrite nanoparticles ZnFe<sub>2-x</sub>Gd<sub>x</sub>O<sub>4</sub> (x = 0.00) show the ferromagnetic behavior with saturation magnetization 5.6 emu g<sup>-1</sup> (at 10,000 Oe applied magnetic field) and coercivity 9.6 Oe, as presented in Table 8. In normal ZnFe<sub>2</sub>O<sub>4</sub>, Zn<sup>2+</sup> occupy all the tetrahedral sites and the Fe<sup>3+</sup> ions occupy octahedral sites with the antiparallel arrangement of magnetic moments, therefore, there is no possibility

of superexchange interaction between the cations at tetrahedral and octahedral site, consequently paramagnetic behavior [47]. At nanoscale of zinc ferrite, Fe<sup>3+</sup> ion migrates to the tetrahedral site and thereby exhibit superexchange interaction between cations at tetrahedral and octahedral sites, therefore, ZnFe<sub>2-x</sub>Gd<sub>x</sub>O<sub>4</sub> (x = 0.00) nanoparticles exhibit ferromagnetic behavior [48]. It can be observed from Fig. 10 and Table 8 that the decrease of saturation magnetization is associated with substitution of Gd<sup>3+</sup> in zinc ferrite nanoparticles. The Gd<sup>3+</sup> ions prefer to occupy octahedral sites due to the larger ionic radius as compare to Fe<sup>3+</sup>. Gadolinium behaves ferromagnetic below the temperature 16 °C, and exhibits paramagnetic at room temperature [49]. Therefore, Gd<sup>3+</sup>-substitution in zinc ferrite nanoparticles is similar to the substitution of non-magnetic ions at octahedral sites in zinc ferrite nanoparticles. The increase of substitution of paramagnetic Gd<sup>3+</sup> at octahedral sites in zinc ferrite nanoparticles, disturbed the superexchange interaction and consequently conversion of magnetic hysteresis curves from ferromagnetic to paramagnetic with a decrease in saturation magnetization as noticed. Similar, conversion of hysteresis curves from ferromagnetic to a paramagnetic with the substitution of Gd<sup>3+</sup> in zinc ferrite nanoparticles synthesized by co-precipitation method, was noticed by Pradeep Raja et al. [9] research group.

### 3.7 Dielectric constant and dielectric loss

The dielectric properties of spinel ferrite are due to electric dipole moments created as a result of charge transfer caused by ion exchange among divalent and trivalent cations within the spinel crystal structure [50]. Figure 11a, b depict the room temperature variation in real part of dielectric constant ( $\epsilon'$ ), imaginary part of dielectric constant ( $\epsilon''$ ) for ZnFe<sub>2-x</sub>Gd<sub>x</sub>O<sub>4</sub> (x = 0.00, 0.05, 0.10, 0.20) nanoparticles measured at room temperature in the frequency range 1 Hz–1 MHz. It can be noticed from Fig. 11a that the value of real part of dielectric constant decreases rapidly with the increase of frequency up to 1 kHz. At higher frequency, it decreases slowly and becomes constant at frequency up to 1 MHz. This dependence of dielectric constant with frequency indicate the usual dielectric dispersion [51]. The sharp decrease in dielectric constant at a lower frequency can be explained on the basis of Koop's phenomenological theory, which assumes the dielectric structure as an inhomogeneous medium of two layers of the Maxwell–Wagner type [52, 53]. In view of this, the dielectric structure of spinel ferrite is considered to be consisting of well-conducting grains, which are alienated by poorly conducting grain boundaries. During hopping process, under an applied ac electric field, electrons have to move through the grains and grain boundaries of the dielectric material. The grain boundaries are more effective at low frequency, whereas, grains are effective at

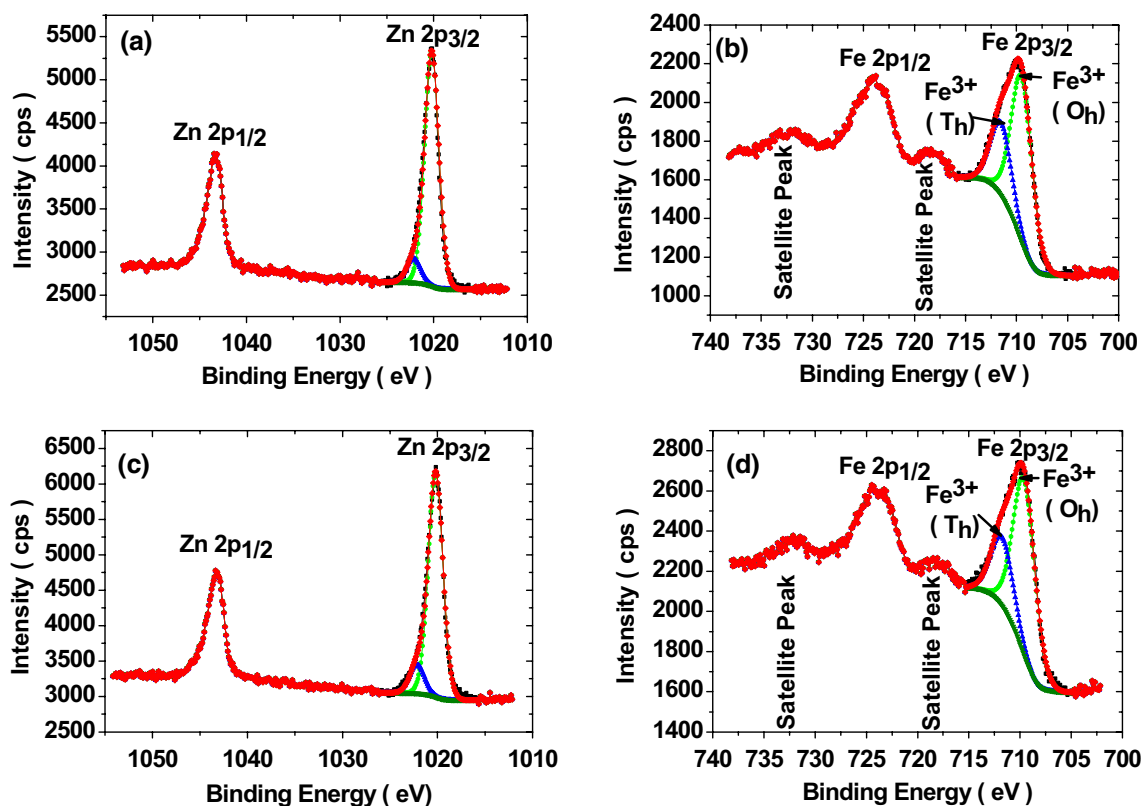


Fig. 9 High resolution XPS spectra: **a** Zn and **b** Fe for  $ZnFe_{2-x}Gd_xO_4$  ( $x=0.00$ ) nanoparticles; **c** Zn and **d** Fe for  $ZnFe_{2-x}Gd_xO_4$  ( $x=0.20$ ) nanoparticles

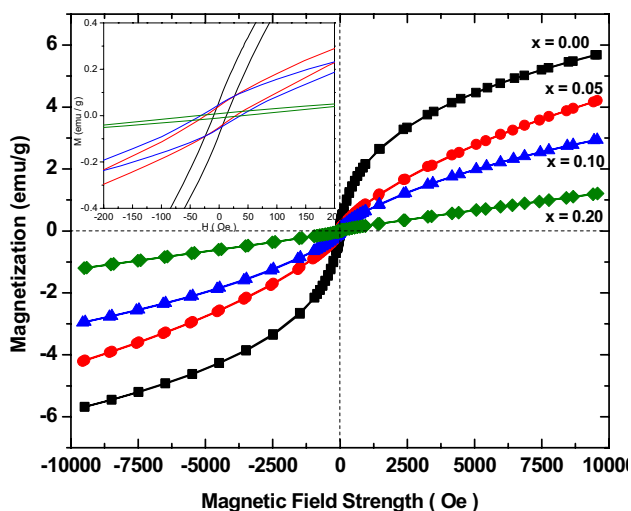


Fig. 10 Hysteresis curves for  $ZnFe_{2-x}Gd_xO_4$  ( $x=0.00, 0.05, 0.10, 0.20$ ) nanoparticles. Inset is enlarge view of hysteresis curves

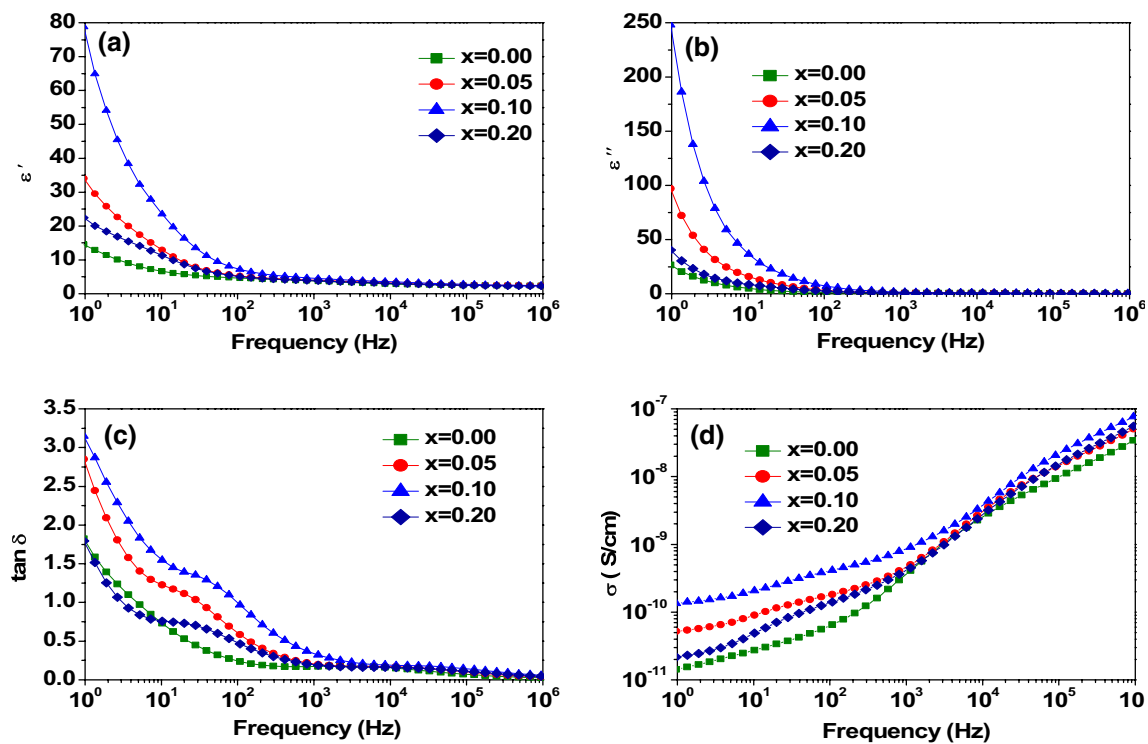
high frequency [54]. Due to the high resistance of grain boundary, electrons accumulate on the grain boundaries and generate space charge polarization, consequently observation of high value of dielectric constant at low frequency

Table 8 Crystallite size, saturation magnetization, coercivity, remanant magnetization,  $M_r/M_s$  ratio for  $ZnFe_{2-x}Gd_xO_4$  ( $x=0.00, 0.05, 0.10, 0.20$ ) nanoparticles

| x    | D (nm) | $M_s$ (emu g <sup>-1</sup> ) | $H_c$ (Oe) | $M_r$ (emu g <sup>-1</sup> ) | $M_r/M_s$ |
|------|--------|------------------------------|------------|------------------------------|-----------|
| 0.00 | 9.2    | 5.6                          | 9.6        | 0.057                        | 0.010     |
| 0.05 | 5.6    | 4.2                          | 20.7       | 0.042                        | 0.010     |
| 0.10 | 4.7    | 2.9                          | 33.4       | 0.047                        | 0.016     |
| 0.20 | 3.6    | 1.2                          | 26.2       | 0.010                        | 0.008     |

[55]. With the increase of frequency, grains come into action and therefore, a sharp decrease in dielectric constant due to the decrease in space charge polarization. Further, at high frequency, hopping of electrons cannot follow the applied ac electric field and consequently frequency independent dielectric constant is noted with  $Gd^{3+}$  substitution in zinc ferrite nanoparticle and presented in Table 9. Similar reports are also available for  $Gd^{3+}$  doped other spinel ferrites [49, 57].

Figure 11c and Table 9 signify the variation of dielectric loss ( $\tan\delta$ ) with variation of frequency (1 Hz–1 MHz) for  $ZnFe_{2-x}Gd_xO_4$  ( $x=0.00, 0.05, 0.10, 0.20$ ) nanoparticles. It can be noticed from Fig. 11c that the dielectric



**Fig. 11** **a** Real part of dielectric constant ( $\epsilon'$ ), **b** imaginary part of dielectric constant ( $\epsilon''$ ), **c** dielectric loss factor ( $\tan\delta$ ), and **d** ac conductivity ( $\sigma$ ) for  $\text{ZnFe}_{2-x}\text{Gd}_x\text{O}_4$  ( $x = 0.00, 0.05, 0.10, 0.20$ ) nanoparticles

**Table 9** Electrical parameters: real part of dielectric constant ( $\epsilon'$ ), imaginary part of dielectric constant ( $\epsilon''$ ), dielectric loss ( $\tan\delta$ ) and ac conductivity ( $\sigma$ ) at 1 Hz and 1 kHz frequency for  $\text{ZnFe}_{2-x}\text{Gd}_x\text{O}_4$  ( $x = 0.00, 0.05, 0.10, 0.20$ ) nanoparticles

| Sample<br>$\text{ZnFe}_{2-x}\text{Gd}_x\text{O}_4$ | $\epsilon'$ |      | $\epsilon''$ |       | $\tan\delta$ |      | $\sigma \times 10^{-10}$<br>( $\text{S cm}^{-1}$ ) |      |
|--|-------------|------|--------------|-------|--------------|------|--|------|
|  | 1 kHz       | 1 Hz | 1 kHz        | 1 Hz  | 1 kHz        | 1 Hz | 1 kHz  | 1 Hz |
| 0.00   | 3.8         | 14.5 | 0.6          | 25.2  | 0.17         | 1.79 | 3.48   | 0.14 |
| 0.05   | 4.0         | 34.2 | 0.8          | 94.8  | 0.21         | 2.84 | 4.51   | 0.52 |
| 0.10   | 4.6         | 77.3 | 1.6          | 245.3 | 0.34         | 3.17 | 8.72   | 1.34 |
| 0.20   | 3.8         | 22.5 | 0.7          | 39.6  | 0.20         | 1.79 | 4.05   | 0.21 |

loss ( $\tan\delta$ ) decreases with the increase of frequency and it is constant or independent at a higher frequency. At low frequency, high resistivity of grain boundaries is more dominant, therefore it results in a high value of dielectric loss at low frequency [58]. In other words, more energy is needed to electron exchange due to the high resistivity of grain boundaries and therefore more energy loss at low frequency. By increasing further frequency, less energy is needed to electron exchange and results in less dielectric loss at a higher frequency [59]. The presence of resonance peak in Fig. 11c can be also noticed for synthesized  $\text{Gd}^{3+}$  substituted zinc ferrite nanoparticles. This appearance of resonance peak is associated with the the jumping frequency of localized electrons at approximately equal to the externally applied ac field. The condition for observing resonance peak in the dielectric loss of spinel

ferrite is  $\omega\tau = 1$ , where  $\omega = 2\pi f$  [60]. At this condition, the power loss is due to the maximum of electrical energy is transferred to oscillating ions.

### 3.8 AC conductivity

Figure 11d and Table 9 illustrate the variation of ac conductivity ( $\sigma$ ) for  $\text{ZnFe}_{2-x}\text{Gd}_x\text{O}_4$  ( $x = 0.00, 0.05, 0.10, 0.20$ ) nanoparticles investigated in the frequency range 1 Hz–1 MHz. It is well known that the decrease in ac conductivity with frequency indicate large polaron hopping, whereas, increase one is linked to small polaron hopping [61]. Therefore, in our present study, the linear increase of ac conductivity, Fig. 11d, specify the small polaron conduction. The observed linear increase in frequency dependent ac conductivity is due to conduction through electron exchange between the ions of the

same element but different valence states in synthesized  $\text{Gd}^{3+}$  substituted  $\text{ZnFe}_2\text{O}_4$  spinel ferrite nanoparticles [62]. Under an applied electric field, this electron exchange increases with the increase of frequency, therefore, increase in ac conductivity of  $\text{Gd}^{3+}$  substituted zinc ferrite nanoparticles. Further, the observed frequency dependent ac conductivity from Fig. 11d, can be find explanation on the basis of the Maxwell–Wagner two-layer model [63]. In view of this model, grain boundaries are more active at lower frequencies, thereby, the hopping frequency of the electrons between  $\text{Fe}^{3+}$  and  $\text{Fe}^{2+}$  ions are low at lower frequencies [64]. With the increase of applied field frequency, the conductive grains become more active, consequently, promotion of electron hopping between two nearby octahedral sites and a transition between  $\text{Fe}^{2+}$  and  $\text{Fe}^{3+}$  ions. Therefore, the ac conductivity gradually increases with the increase of frequency for synthesized  $\text{Gd}^{3+}$  ion substituted  $\text{ZnFe}_2\text{O}_4$  spinel ferrite nanoparticles [65]. The addition of  $\text{Gd}^{3+}$  ions in zinc ferrite nanoparticles results in change of crystallite size and cation redistribution at the octahedral site. Furthermore, this impact of  $\text{Gd}^{3+}$  ion in zinc ferrite nanoparticles influenced the hopping of charge carriers and consequently the ac conductivity of synthesized spinel ferrite nanoparticles [66].

### 3.9 Modulus spectroscopy

Modulus spectroscopy is a characterization tool to analyse the electrical relaxation of spinel ferrite nanoparticles for distinguishing the role of grain and grain boundary [67]. The electric complex modulus  $M^*$  is defined as the reciprocal of complex permittivity (dielectric constant)  $\epsilon^*$  [68]:

$$M^* = \frac{1}{\epsilon^*} = \frac{\epsilon'}{\epsilon'^2 + \epsilon''^2} + j \frac{\epsilon''}{\epsilon'^2 + \epsilon''^2} = M' + jM''$$

where  $M'$  and  $M''$  are real and imaginary part of the electric complex modulus  $M^*$ . Figure 12a illustrates the variation of  $M'$  with frequency for  $\text{ZnFe}_{2-x}\text{Gd}_x\text{O}_4$  ( $x = 0.00, 0.05, 0.10, 0.20$ ) nanoparticles. It can be noticed from Fig. 12a that  $M'$  is approximately zero at low frequency, whereas, it has increasing dispersion with the increase of frequency. Moreover, at low frequency,  $M'$  value near to zero, which specify the negligible value of electronic polarization [7]. It can be observed that  $M'$  has a bent to saturate at a maximum value due to relaxation process at the high-frequency region. At high frequency, the value of  $M'$  increases rapidly with the increase of frequency, which remarks conduction mechanism is due to short range movement of charge carriers [69]. Figure 12b represents the variation of  $M''$  with frequency for  $\text{ZnFe}_{2-x}\text{Gd}_x\text{O}_4$  ( $x = 0.00, 0.05, 0.10, 0.20$ ) nanoparticles. It can be perceived from Fig. 12b that there are two broad peaks related to relaxation process, which are the contribution from grains and grain boundaries [70]. The observed relaxation peak at low-frequency region is the

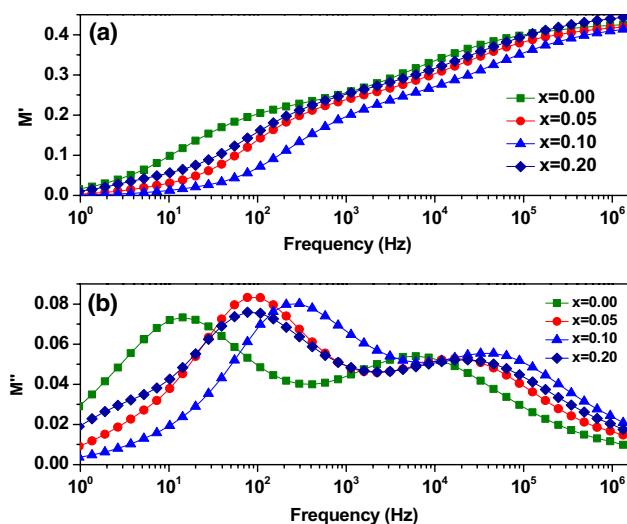


**Fig. 12** **a** Real part of electric modulus  $M'$  and **b** imaginary part of electric modulus  $M''$  as a function of variable frequency for  $\text{ZnFe}_{2-x}\text{Gd}_x\text{O}_4$  ( $x = 0.00, 0.05, 0.10, 0.20$ ) nanoparticles

contribution of grain boundaries and one at high-frequency region is related to contribution of grains. The grain boundaries exhibit high resistance and low capacitance than those of grains, and therefore, the resistance of grain boundaries contributed to semicircle region at low-frequency, however, at high-frequency the semicircle region is the contribution due to grains [71]. Moreover,  $M''$  peak at the low-frequency side reflects the region in which charge carriers can mobile over long distances. However, the high-frequency side of  $M''$  peak specifies the range in which charge carriers are spatially confined to their potential wells, i.e., charge carriers can move over short distances [72]. The variation in  $M''$  peak frequency position with the variation of  $\text{Gd}^{3+}$  content in spinel ferrite nanoparticles can be perceived from Fig. 12b. The characteristic frequency at which  $M''$  is maximum ( $M''_{\max}$ ) specifies relaxation frequency and it is utilized to evaluate relaxation time ( $\tau$ ) through following relation [73]:

$$\tau_{M''} = \frac{1}{2\pi f_{M''}}$$

The evaluated value of relaxation time corresponding to the contribution of grain ( $\tau_g$ ) and grain boundaries ( $\tau_{gb}$ ) are presented in Table 10. Further,  $M''$  has an inverse relation with capacitance,  $C$ , by following relation [74]:

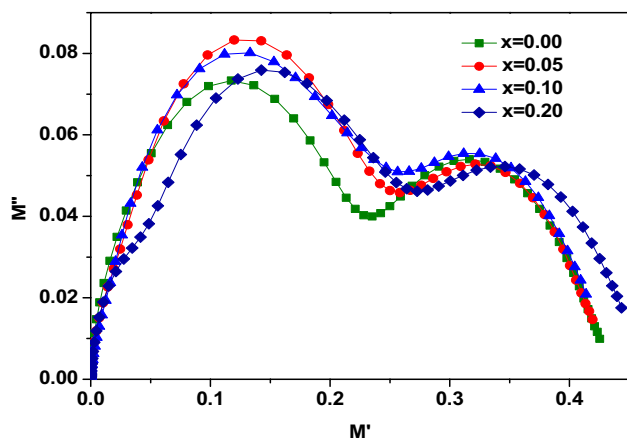
$$M'' = \frac{\epsilon_0}{2C}$$

The resistance value can be evaluated by using following relation with maximum frequency ( $f_{\max}$ ) and capacitance ( $C$ ) [75]:

$$2\pi f_{\max} RC = 1$$

**Table 10** Electrical parameters: grain relaxation time ( $\tau_g$ ), grain boundary relaxation time ( $\tau_{gb}$ ), grain resistance ( $R_g$ ), grain boundary resistance ( $R_{gb}$ ), grain capacitance ( $C_g$ ) and grain boundary capacitance ( $C_{gb}$ ) for  $\text{ZnFe}_{2-x}\text{Gd}_x\text{O}_4$  ( $x=0.00, 0.05, 0.10, 0.20$ ) nanoparticles

| Sample $\text{ZnFe}_{2-x}\text{Gd}_x\text{O}_4$ | $\tau_g$ ( $\mu\text{s}$ ) | $\tau_{gb}$ ( $\mu\text{s}$ ) | $R_g$ (k $\Omega$ ) | $R_{gb}$ (k $\Omega$ ) | $C_g$ (pF) | $C_{gb}$ (pF) |
|---|----------------------------|-------------------------------|---------------------|------------------------|------------|---------------|
| 0.00  | 25.7                       | 11,513                        | 317.0               | $18.9 \times 10^4$     | 81.3       | 60.7          |
| 0.05  | 6.9                        | 1860                          | 81.4                | $3.5 \times 10^4$      | 84.7       | 52.7          |
| 0.10  | 2.9                        | 620                           | 37.1                | $1.1 \times 10^4$      | 80.7       | 56.1          |
| 0.20  | 6.6                        | 2070                          | 78.8                | $3.6 \times 10^4$      | 83.9       | 58.3          |

**Fig. 13** Cole–Cole plots for spinel ferrite  $\text{ZnFe}_{2-x}\text{Gd}_x\text{O}_4$  ( $x=0.00, 0.05, 0.10, 0.20$ ) nanoparticles

The calculated value of grain resistance ( $R_g$ ), grain boundary resistance ( $R_{gb}$ ), grain capacitance ( $C_g$ ), and grain boundary capacitance ( $C_{gb}$ ) are presented in Table 10. These electrical parameters have the variation with  $\text{Gd}^{3+}$  substitution and crystallite size of zinc ferrite nanoparticles. These effects were consistent with previous studies on spinel ferrite nanoparticles [76].

Figure 13 depicts Cole–Cole plots for spinel ferrite  $\text{ZnFe}_{2-x}\text{Gd}_x\text{O}_4$  ( $x=0.00, 0.05, 0.10, 0.20$ ) nanoparticles. It can be perceived from Cole–Cole plots that it contains two successive semicircles. The first semicircle at low frequency specifies the contribution of grain boundaries and the second semicircle at high frequency provides the contribution of grains to conduction mechanism. The presence of two semicircles in Cole–Cole plots specifies the role of both grains and grain boundaries to conduction process in synthesized  $\text{Gd}^{3+}$  ion substituted zinc ferrite nanoparticles.

## 4 Conclusion

In summary,  $\text{ZnFe}_{2-x}\text{Gd}_x\text{O}_4$  ( $x=0.00, 0.05, 0.10, 0.20$ ) spinel ferrite nanoparticles were successfully synthesized by honey mediated sol–gel auto-combustion method. By variation of  $\text{Gd}^{3+}$  ion substitution level in zinc ferrite nanoparticles, we

investigated the changes in structural, magnetic, dielectric and electrical properties. X-ray diffraction, Raman Spectroscopy and Fourier Transform Infrared Spectroscopy confirmed the formation of spinel ferrite crystal structure of synthesized  $\text{ZnFe}_{2-x}\text{Gd}_x\text{O}_4$  ( $x=0.00, 0.05, 0.10, 0.20$ ) nanoparticles. Magnetic properties of synthesized spinel ferrite nanoparticles were investigated by vibrating sample magnetometer at room temperature. The conversion of magnetic hysteresis curves for synthesized  $\text{ZnFe}_{2-x}\text{Gd}_x\text{O}_4$  ( $x=0.00, 0.05, 0.10, 0.20$ ) nanoparticles from ferromagnetic to a paramagnetic with the substitution of  $\text{Gd}^{3+}$  in zinc ferrite nanoparticles was observed. The increase of substitution of paramagnetic  $\text{Gd}^{3+}$  ions at octahedral sites in zinc ferrite nanoparticles, disturbed the super-exchange interaction and as a result conversion of magnetic hysteresis curves from ferromagnetic to paramagnetic with a decrease in saturation magnetization was noticed. The substitution of  $\text{Gd}^{3+}$  ions in zinc ferrite nanoparticles resulted a change in crystallite size and cation redistribution at the octahedral site. The presence of  $\text{Zn}^{2+}$  and  $\text{Fe}^{3+}$  oxidation state in synthesized nanoparticles was confirmed by X-ray photoelectron spectroscopy. Further, the change in dielectric constant was observed with  $\text{Gd}^{3+}$  substitution in zinc ferrite nanoparticle. The  $\text{Gd}^{3+}$  ion substitution in zinc ferrite nanoparticles also influenced the hopping of charge carriers and consequently the ac conductivity of synthesized spinel ferrite nanoparticles. The occurrence of two semicircles in Cole–Cole plot confirmed the role of both grains and grain boundaries to conduction process in synthesized  $\text{Gd}^{3+}$  ion substituted zinc ferrite nanoparticles. Furthermore, the grain relaxation time ( $\tau_g$ ), grain boundary relaxation time ( $\tau_{gb}$ ), grain resistance ( $R_g$ ), grain capacitance ( $C_g$ ), grain boundary resistance ( $R_{gb}$ ) and grain boundary capacitance ( $C_{gb}$ ) for synthesized  $\text{ZnFe}_{2-x}\text{Gd}_x\text{O}_4$  ( $x=0.00, 0.05, 0.10, 0.20$ ) nanoparticles were evaluated through Modulus Spectroscopy. The variation in evaluated electrical parameters demonstrated the impact of  $\text{Gd}^{3+}$  substitution in zinc ferrite nanoparticles.

**Acknowledgements** This work was supported by the Ministry of Education, Youth and Sports of the Czech Republic—Program NPU I (LO1504). One author ‘Milan Masar’ also acknowledges an internal Grant IGA/CPS/2017/7 from TBU in Zlín.

## References

1. S.M. Ansari, R.D. Bhor, K.R. Pai, S. Mazumder, D. Sen, Y.D. Kolekar, C.V. Ramana, Size and chemistry controlled cobalt–ferrite nanoparticles and their anti-proliferative effect against the MCF-7 breast cancer cells. *ACS Biomater. Sci. Eng.* **2**, 2139–2152 (2016)
2. P.P. Goswami, H.A. Choudhury, S. Chakma, V.S. Moholkar, Sonochemical synthesis and characterization of manganese ferrite nanoparticles. *Ind. Eng. Chem. Res.* **52**, 17848–17855 (2013)
3. X. Zeng, J. Zhang, S. Zhu, X. Deng, H. Ma, J. Zhang, Q. Zhang, P. Li, D. Xue, N.J. Mellors, X. Zhang, Y. Peng, Direct observation of cation distributions of ideal inverse spinel  $\text{CoFe}_2\text{O}_4$  nanofibres and correlated magnetic properties. *Nanoscale* **8**, 7493–7500 (2017)
4. S.G. Kakade, R.C. Kambale, C.V. Ramanna, Y.D. Kolekar, Crystal strain, chemical bonding, magnetic and magnetostrictive properties of erbium ( $\text{Er}^{3+}$ ) ion substituted cobalt-rich ferrite ( $\text{Co}_{1-x}\text{Fe}_{1.9-x}\text{Er}_x\text{O}_4$ ). *RSC Adv.* **6**, 33308–33317 (2016)
5. G. Xi, L. Wang, T. Zhao, Magnetic and magnetostrictive properties of RE-doped Cu–Co ferrite fabricated from spent lithium-ion batteries. *J. Magn. Magn. Mater.* **424**, 130–136 (2017)
6. C. Virlan, G. Bulai, O.F. Caltun, R. Hempelmann, A. Pui, Rare earth metals' influence on the heat generating capability of cobalt ferrite nanoparticles. *Ceram. Int.* **42**, 11958–11965 (2016)
7. L. Chauhan, N. Singh, A. Dhar, H. Kumar, S. Kumar, K. Sreenivas, Structural and electrical properties of  $\text{Dy}^{3+}$  substituted  $\text{NiFe}_2\text{O}_4$  ceramics prepared from powders derived by combustion method. *Ceram. Int.* **43**, 8378–8390 (2017)
8. M. Bini, C. Tondo, M. Capsoni, M.C. Mozzati, B. Albin, P. Galinetto, Superparamagnetic  $\text{ZnFe}_2\text{O}_4$  nanoparticles: the effect of Ca and Gd doping. *Mater. Chem. Phys.* **204**, 72–82 (2018)
9. P. Raja, T. Yadavalli, D. Ravi, H.A. Therese, C. Ramasamy, Y. Hayakawa, Synthesis and magnetic properties of gadolinium substituted zinc ferrites. *Mater. Lett.* **188**, 406–408 (2017)
10. J. Peng, M. Hojamberdiev, Y. Xu, B. Cao, J. Wang, H. Wu, Hydrothermal synthesis and magnetic properties of gadolinium-doped  $\text{CoFe}_2\text{O}_4$  nanoparticles. *J. Magn. Magn. Mater.* **323**, 133–138 (2011)
11. S. Amiri, H. Shokrollahi, Magnetic and structural properties of RE doped Co-ferrite (RE = Nd, Eu, and Gd) nano-particles synthesized by co-precipitation. *J. Magn. Magn. Mater.* **345**, 18–23 (2013)
12. P. Samoila, L. Sacarescu, A.I. Borhan, D. Timpu, M. Grigoras, N. Lupu, M. Zaltariov, V. Harabagiu, Magnetic properties of nanosized Gd–Mn–Cr ferrites prepared using the sol–gel auto-combustion technique. *J. Magn. Magn. Mater.* **378**, 92–97 (2015)
13. Z.Z. Lazarevic, C. Jovalekic, A. Milutinovic, D. Sekulic, V.N. Ivanovski, A. Recnik, B. Cekic, N.Z. Romcevic, Nanodimensional spinel  $\text{NiFe}_2\text{O}_4$  and  $\text{ZnFe}_2\text{O}_4$  ferrites prepared by soft mechanochemical synthesis. *J. Appl. Phys.* **113**, 187221 (2013)
14. J. Borchering, J. Baltrusaitis, H. Chen, L. Stebounova, C.-M. Wu, G. Rubasinghege, I.A. Mudunkotuwa, J.C. Caraballo, J. Zabner, V.H. Grassian, A.P. Comellas, Iron oxide nanoparticles induce *Pseudomonas aeruginosa* growth, induce biofilm formation, and inhibit antimicrobial peptide function. *Environ. Sci. Nano* **1**(2), 123–132 (2015). <https://doi.org/10.1039/C3EN00029J>
15. B.D. Cullity, *Elements of X-ray Diffraction* (Addison-Wesley, New York, 1956), p. 139
16. A. Kumar, P.S. Rana, M.S. Yadav, R.P. Pant, Effect of  $\text{Gd}^{3+}$  ion distribution on structural and magnetic properties in nano-sized Mn–Zn ferrite particles. *Ceram. Int.* **41**, 1297–1302 (2015)
17. P. Vanysek, *CRC Handbook of Chemistry and Physics* (CRC Press, Boca Raton, 2001)
18. S. Joshi, M. Kumar, S. Chhoker, A. Kumar, M. Singh, Effect of  $\text{Gd}^{3+}$  substitution on structural, magnetic, dielectric and optical properties of nanocrystalline  $\text{CoFe}_2\text{O}_4$ . *J. Magn. Magn. Mater.* **426**, 252–263 (2017)
19. C. Pereira, A.M. Pereira, C. Fernandes, M. Rocha, R. Mendes, M.P. Fernandez-García, A. Guedes, P.B. Tavares, J.-M. Grenèche, J.P. Araujo, C. Freire, Superparamagnetic  $\text{MFe}_2\text{O}_4$  (M = Fe, Co, Mn) nanoparticles: tuning the particle size and magnetic properties through a novel one-step coprecipitation route. *Chem. Mater.* **24**, 1496–1504 (2012)
20. C. Singh, A. Goyal, S. Singhal, Nickel-doped cobalt ferrite nanoparticles: efficient catalysts for the reduction of nitroaromatic compounds and photo-oxidative degradation of toxic dyes. *Nanoscale* **6**, 7959–7970 (2014)
21. D.S. Nikam, S.V. Jadhav, V.M. Khot, R.A. Bohara, C.K. Hong, S.S. Mali, S.H. Pawar, Cation distribution, structural, morphological and magnetic properties of  $\text{Co}_{1-x}\text{Zn}_x\text{Fe}_2\text{O}_4$  ( $x = 0-1$ ) nanoparticles. *RSC Adv.* **5**, 2338 (2015)
22. S. Kumari, V. Kumar, P. Kumar, M. Kar, L. Kumar, Structural and magnetic properties of nanocrystalline yttrium substituted cobalt ferrite synthesized by the citrate precursor technique. *Adv. Powder Technol.* **26**, 213–223 (2015)
23. B. Parvatheeswara Rao, B. Dhanalakshmi, S. Ramesh, P.S.V. Subba Rao, Cation distribution of Ni–Zn–Mn ferrite nanoparticles. *J. Magn. Magn. Mater.* **456**, 444–450 (2018)
24. P.P. Naik, R.B. Tangsali, S.S. Meena, S.M. Yusuf, Influence of rare earth ( $\text{Nd}^{3+}$ ) doping on structural and magnetic properties of nanocrystalline manganese-zinc ferrite. *Mater. Chem. Phys.* **191**, 215–224 (2017)
25. Z. Yan, J. Luo, Effects of Ce–Zn co-substitution on structure, magnetic and microwave absorption properties of nickel ferrite nanoparticles. *J. Alloys Compd.* **695**, 1185–1195 (2017)
26. V.J. Angadi, L. Choudhury, K. Sadhana, H.-L. Liu, R. Sandhya, S. Matteppanavar, B. Rudraswamy, V. Pattar, R.V. Anavekar, K. Praveena, Structural, electrical and magnetic properties of  $\text{Sc}^{3+}$  doped Mn–Zn ferrite nanoparticles. *J. Magn. Magn. Mater.* **424**, 1–11 (2017)
27. A. Thakur, P. Kumar, P. Thakur, K. Rana, A. Chevalier, J.-L. Mattei, P. Queffelec, Enhancement of magnetic properties of  $\text{Ni}_{0.5}\text{Zn}_{0.5}\text{Fe}_2\text{O}_4$  nanoparticles prepared by the co-precipitation method. *Ceram. Int.* **42**, 10664–10670 (2016)
28. S.T. Assar, H.F. Abosheisha, Effect of Ca substitution on some physical properties of nano-structured and bulk Ni-ferrite samples. *J. Magn. Magn. Mater.* **374**, 264–272 (2015)
29. S. Bhukal, M. Dhiman, S. Bansal, M.K. Tripathi, S. Singhal, Substituted Co–Cu–Zn nanoferrites: synthesis, fundamental and redox catalytic properties for the degradation of methyl orange. *RSC Adv.* **6**, 1360–1375 (2016)
30. K.R. Babu, K.R. Rao, B.R. Babu,  $\text{Cu}^{2+}$ -modified physical properties of cobalt-nickel ferrite. *J. Magn. Magn. Mater.* **434**, 118–125 (2017)
31. S. Torkian, A. Ghasemi, R.S. Razavi, Cation distribution and magnetic analysis of wideband microwave absorptive  $\text{Co}_x\text{Ni}_{1-x}\text{Fe}_2\text{O}_4$  ferrites. *Ceram. Int.* **43**, 6987–6995 (2017)
32. M.A. Amer, T. Meaz, A. Hashhash, S. Attalah, F. Fakhry, Structural phase transformations of as-synthesized Cu-nanoferrites by annealing process. *J. Alloys Compd.* **649**, 712–720 (2015)
33. H.M. Zaki, H.A. Dawoud, Far-infrared spectra for copper–zinc mixed ferrites. *Physica B* **405**, 4476–4479 (2010)
34. P. Choudhary, D. Varshney, Elucidation of structural, vibrational and dielectric properties of transition metal ( $\text{Co}^{2+}$ ) doped spinel Mg–Zn chromites. *J. Magn. Magn. Mater.* **454**, 274–288 (2018)
35. J. Singh, A. Roychoudhury, M. Srivastava, V. Chaudhary, R. Prasanna, D.W. Lee, S.H. Lee, B.D. Malhotra, Highly efficient bienzyme functionalized biocompatible nanostructured nickel ferrite-chitosan nanocomposite platform for biomedical application. *J. Phys. Chem.* **117**, 8491–8502 (2013)

36. D. Varshney, K. Verma, A. Kumar, Substitutional effect on structural and magnetic properties of  $A_x\text{Co}_{1-x}\text{Fe}_2\text{O}_4$  ( $A = \text{Zn, Mg}$  and  $x = 0.0, 0.5$ ) ferrites. *J. Mol. Struct.* **1006**, 447–452 (2011)
37. Z. Yan, J. Gao, Y. Li, M. Zhang, M. Guo, Hydrothermal synthesis and structure evolution of metal-doped magnesium ferrite from saprolite laterite. *RSC Adv.* **5**, 92778–92787 (2015)
38. S. Thota, S.C. Kashyap, S.K. Sharma, V.R. Reddy, Cation distribution in Ni-substituted  $\text{Mn}_{0.5}\text{Zn}_{0.5}\text{Fe}_2\text{O}_4$  nanoparticles: a Raman, Mössbauer, X-ray diffraction and electron spectroscopy study. *Mater. Sci. Eng., B* **206**, 69–78 (2016)
39. R.N. Bhowmik, A.K. Sinha, Improvement of room temperature electric polarization and ferrimagnetic properties of  $\text{Co}_{1.25}\text{Fe}_{1.75}\text{O}_4$  ferrite by heat treatment. *J. Magn. Magn. Mater.* **421**, 120–131 (2017)
40. L. Wang, X. Lu, C. Han, R. Lu, S. Yang, X. Song, Electrospun hollow cage-like  $\alpha\text{-Fe}_2\text{O}_3$  microspheres: synthesis, formation mechanism, and morphology-preserved conversion to Fe nanostructures. *CrystEngComm.* **16**, 10618–10623 (2014)
41. R.A. Pawar, S.M. Patange, Q.Y. Tamboli, V. Ramanathan, S.E. Shirsath, Spectroscopic, elastic and dielectric properties of  $\text{Ho}^{3+}$  substituted Co–Zn ferrites synthesized by sol–gel method. *Ceram. Int.* **42**, 16096–16102 (2016)
42. J. Zhang, J.-M. Song, H.-L. Niu, C.-J. Mao, S.-Y. Zhang, Y.-H. Shen,  $\text{ZnFe}_2\text{O}_4$  nanoparticles: synthesis, characterization, and enhanced gassing property for acetone. *Sens. Actuators B* **221**, 55–62 (2015)
43. X. Guo, H. Zhu, M. Si, C. Jiang, D. Xue, Z. Zhang, Q. Li,  $\text{ZnFe}_2\text{O}_4$  nanotubes: microstructure and magnetic properties. *J. Phys. Chem. C* **118**, 30145–30152 (2014)
44. G.H. Jaffari, A.K. Rumaiz, J.C. Woicik, S.I. Shah, Influence of oxygen vacancies on the electronic structure and magnetic properties of  $\text{NiFe}_2\text{O}_4$  thin films. *J. Appl. Phys.* **111**, 093906 (2012)
45. A. Hao, M. Ismail, S. He, N. Qin, R. Chen, A.M. Rana, D. Bao, Enhanced resistive switching and magnetic properties of Gd-doped  $\text{NiFe}_2\text{O}_4$  thin films prepared by chemical solution deposition method. *Mater. Sci. Eng. B* **229**, 86–95 (2018)
46. M.A. Dar, D. Varshney, Effect of d-block element  $\text{Co}^{2+}$  substitution on structural, Mössbauer and dielectric properties of spinel copper ferrites. *J. Magn. Magn. Mater.* **436**, 101–112 (2017)
47. Z.Z. Lazarević, Č. Jovalekić, V.N. Ivanovski, A. Rečnik, A. Milutinović, B. Cekić, N. Romčević, Characterization of partially inverse spinel  $\text{ZnFe}_2\text{O}_4$  with high saturation magnetization synthesized via soft mechanochemically assisted route. *J. Phys. Chem. Solids* **75**, 869–877 (2014)
48. S. Ayyappan, S. Philip Raja, C. Venkateswaran, J. Philip, B. Raj, Room temperature ferromagnetism in vacuum annealed  $\text{ZnFe}_2\text{O}_4$  nanoparticles. *Appl. Phys. Lett.* **96**, 143106 (2010)
49. R. Islam, M.A. Hakim, M.O. Rahman, H. Narayan Das, M.A. Mamun, Study of the structural, magnetic and electrical properties of Gd-substituted Mn–Zn mixed ferrites. *J. Alloys Compd.* **559**, 174–180 (2013)
50. J. Parashar, V.K. Saxena, D. Jyoti, K.B. Bhatnagar, Sharma, Dielectric behaviour of Zn substituted Cu nano-ferrites. *J. Magn. Magn. Mater.* **394**, 105–110 (2015)
51. C.V. Ramana, Y.D. Kolekar, K. Kamala Bharathi, B. Sinha, K. Ghosh, Correlation between structural, magnetic, and dielectric properties of manganese substituted cobalt ferrite. *J. Appl. Phys.* **114**, 183907 (2013)
52. B.P. Jacob, S. Thankachan, S. Xavier, E.M. Mohammed, Dielectric behavior and AC conductivity of  $\text{Tb}^{3+}$  doped  $\text{Ni}_{0.4}\text{Zn}_{0.6}\text{Fe}_2\text{O}_4$  nanoparticles. *J. Alloys Compd.* **541**, 29–35 (2012)
53. M. Ahmad, M. Azhar Khan, A. Mahmood, S.-S. Liu, A.H. Chughtai, W.-C. Cheong, B. Akram, G. Nasar, Role of ytterbium on structural and magnetic properties of  $\text{NiCr}_{0.1}\text{Fe}_{1.9}\text{O}_4$  co-precipitated ferrites. *Ceram. Int.* **44**, 5433–5439 (2018)
54. A.A. Kadam, S.S. Shinde, S.P. Yadav, P.S. Patil, K.Y. Rajpure, Structural, morphological, electrical and magnetic properties of Dy doped Ni–Co substitutional spinel ferrite. *J. Magn. Magn. Mater.* **329**, 59–64 (2013)
55. D. Varshney, K. Verma, Substitutional effect on structural and dielectric properties of  $\text{Ni}_{1-x}\text{A}_x\text{Fe}_2\text{O}_4$  ( $A = \text{Mg, Zn}$ ) mixed spinel ferrites. *Mater. Chem. Phys.* **140**, 412–418 (2013)
56. A. Manzoor, M.A. Khan, M.Y. Khan, M.N. Akhtar, A. Hussain, Tuning magnetic and high frequency dielectric behavior in Li–Zn ferrites by Ho doping. *Ceram. Int.* **44**, 6321–6329 (2018)
57. R.R. Kanna, N. Lenin, K. Sakthipandi, A.S. Kumar, Structural, optical, dielectric and magnetic studies of gadolinium-added Mn–Cu nanoferrites. *J. Magn. Magn. Mater.* **453**, 78–90 (2018)
58. R.G. Kharabe, R.S. Devan, C.M. Kanamadi, B.K. Chougule, Dielectric properties of mixed Li–Ni–Cd ferrites, *Smart Mater. Struct.* **15**, N36–N39 (2006). <https://doi.org/10.1088/0964-1726/15/2/N02>
59. S.A. Saafan, S.T. Assar, Dielectric behavior of nano-structured and bulk  $\text{LiNiZn}$  ferrite samples, *J. Magn. Magn. Mater.* **324**, 2989–3001 (2012)
60. Y.D. Kolekar, L.J. Sanchez, C.V. Ramana, Dielectric relaxations and alternating current conductivity in manganese substituted cobalt ferrite. *J. Appl. Phys.* **115**, 144106 (2014)
61. S.G. Kakade, Y.-R. Ma, R.S. Devan, Y.D. Kolekar, C.V. Ramana, Dielectric, complex impedance, and electrical transport properties of erbium ( $\text{Er}^{3+}$ ) ion-substituted nanocrystalline, cobalt-rich ferrite ( $\text{Co}_{1.1}\text{Fe}_{1.9-x}\text{Er}_x\text{O}_4$ ). *J. Phys. Chem. C* **120**, 5682–5693 (2016)
62. A. Manzoor, M.A. Khan, M. Shahid, M.F. Warsi, Investigation of structural, dielectric and magnetic properties of Ho substituted nanostructured lithium ferrites synthesized via auto-citric combustion route. *J. Alloy Compd.* **710**, 547–556 (2017)
63. M.N. Akhtar, M.A. Khan, M.R. Raza, M. Ahmad, G. Murtaza, R. Raza, S.F. Shaikat, M.H. Asif, M. Saleem, M.S. Nazir, Structural, morphological, dielectric and magnetic characterizations of  $\text{Ni}_{0.6}\text{Cu}_{0.2}\text{Zn}_{0.2}\text{Fe}_2\text{O}_4$  (NCZF/MWCNTs/PVDF) nanocomposites for multilayer chip inductor (MLCI) applications. *Ceram. Int.* **40**, 15821–15829 (2014)
64. K.K. Bharathi, G. Markandeyulu, C.V. Ramana, Structural, magnetic, electrical, and magnetoelectric properties of Sm- and Ho-substituted nickel ferrites. *J. Phys. Chem. C* **115**, 554–560 (2011)
65. Z. Liu, Z. Peng, C. Lv, X. Fu, Doping effect of  $\text{Sm}^{3+}$  on magnetic and dielectric properties of Ni–Zn ferrites. *Ceram. Int.* **43**, 1449–1454 (2017)
66. M.T. Rahman, M. Vargas, C.V. Ramana, Structural characteristics, electrical conduction and dielectric properties of gadolinium substituted cobalt ferrite, *J. Alloy Compd.* **617**, 547–562 (2014)
67. M.D. Rahaman, T. Nusrat, R. Maleque, A.K.M. Akther Hossain, Investigation of structural, morphological and electromagnetic properties of  $\text{Mg}_{0.25}\text{Mn}_{0.25}\text{Zn}_{0.5-x}\text{Sr}_x\text{Fe}_2\text{O}_4$  ferrites, *J. Magn. Magn. Mater.* **451**, 391–406 (2018)
68. S.F. Mansour, M.A. Abdo, Electrical modulus and dielectric behavior of  $\text{Cr}^{3+}$  substituted Mg–Zn nanoferrites, *J. Magn. Magn. Mater.* **428**, 300–305 (2017)
69. A.K. Pradhan, T.K. Nath, S. Saha, Impedance spectroscopy and electric modulus behaviour of molybdenum doped cobalt–zinc ferrite. *Mater. Res. Express* **4**, 076107 (2017)
70. W. Chen, W. Zhu, O.K. Tan, X.F. Chen, Frequency and temperature dependent impedance spectroscopy of cobalt ferrite composite thick films. *J. Appl. Phys.* **108**, 034101 (2010)
71. A. Manzoora, M.A. Khan, M.Y. Khan, M.N. Akhtar, A. Hussain, Tuning magnetic and high frequency dielectric behavior in Li–Zn ferrites by Ho doping. *Ceram. Int.* **44**, 6321–6329 (2018)
72. M.A. Ali, M.M. Uddin, M.N.I. Khan, F.-U.-Z. Chowdhury, S.M. Haque, Structural, morphological and electrical properties of

- Sn-substituted Ni–Zn ferrites synthesized by double sintering technique. *J. Magn. Magn. Mater.* **424**, 148–154 (2017)
73. E. Oumezzine, S. Hcini, F.I.H. Rhouma, M. Oumezzine, Frequency and temperature dependence of conductance, impedance and electrical modulus studies of  $\text{Ni}_{0.6}\text{Cu}_{0.4}\text{Fe}_2\text{O}_4$  spinel ferrite. *J. Alloy Compd.* **726**, 187–194 (2017)
74. K. Rasool, M.A. Rafiq, M. Ahmad, Z. Imran, M.M. Hasan,  $\text{TiO}_2$  nanoparticles and silicon nanowires hybrid device: role of interface on electrical, dielectric, and photodetection properties. *Appl. Phys. Lett.* **101**, 253104 (2012)
75. D.C. Sinclair, A.R. West, Impedance and modulus spectroscopy of semiconducting  $\text{BaTiO}_3$  showing positive temperature coefficient of resistance. *J. Appl. Phys.* **66**(8), 3850–3856 (1989)
76. N. Kumari, V. Kumar, S.K. Singh, Structural, dielectric and magnetic investigations on  $\text{Al}^{3+}$  substituted Zn-ferrospinel. *RSC Adv.* **5**, 37925 (2015)